Catalysis Science & Technology

ROYAL SOCIETY OF CHEMISTRY

PAPER

View Article Online
View Journal | View Issue

Cite this: *Catal. Sci. Technol.*, 2025, 15, 5384

Multifunctional $Ti_3C_2T_x$ MXene/carbon nanotube interlayer as a polysulfide electrocatalyst with a high sulfur loading cathode in pre-lithiation Si/S batteries†

Maryam Sadat Kiai, [ab] Navid Aslfattahi, *[c] Deniz Karatas, [d] Nilgun Baydogan,[e] Lingenthiran Samylingam,[f] Kumaran Kadirgama*[ghi] and Chee Kuang Kok[f]

Received 5th June 2025,
Accepted 22nd July 2025

DOI: 10.1039/d5cy00674k

rsc.li/catalysis

A significant area of current research is on the advancement of high-capacity anodes that exhibit outstanding high-rate cycling performance for the next generation of sulfur-based batteries. This study introduces an innovative method for fabricating $Ti_3C_2T_x$ MXene/CNT interlayers through the application of sonication and filtration techniques. In this investigation, carbon nanotubes (CNTs) were employed due to their remarkable mechanical strength and superior electrical conductivity for the high-rate performance of $Ti_3C_2T_x$ coating on glass fiber separators. By integrating the horizontal $Ti_3C_2T_x$ layers and establishing a conductive network on the surface, CNTs reinforce the internal structure and mitigate the shuttle effect in pre-lithiation Si–S batteries. Following 500 cycles, the pre-lithiation S–S battery featuring a $Ti_3C_2T_x$ MXene/CNT interlayer retains approximately 85% of its capacity. Thanks to the distinctive architecture of $Ti_3C_2T_x$/CNT, the battery achieves a reversible capacity of 1047 mAh g^{-1} at a rate of 0.5 C and an impressive capacity of 1207.3 mAh g^{-1} at a rate of 0.2 C. The capability of the $Ti_3C_2T_x$/CNT to recover to 1027 and 1091 mAh g^{-1}, respectively, when the current rate is suddenly altered from 1.0 C to 0.5 C and 0.2 C, demonstrates the structural integrity of the interlayer and its effective lithium polysulfide (LiPS) adsorption properties.

Introduction

Significant progress has been made in creating next-generation batteries that perform far better than current lithium-ion batteries (LIBs). Because sulfur has several advantages, including a high theoretical capacity of 1675 mAh g^{-1}, widespread availability in the earth's crust, and environmentally benign properties, lithium–sulfur (Li–S) batteries have been identified as particularly advantageous among the various alternatives. However, there are significant challenges in the real-world implementation of Li–S batteries. The creation of highly soluble polysulfides during charge–discharge cycles is a major problem because they move between the cathode and anode and cause a significant loss of active material as well as a decrease in capacity.[1–4] The real capacity and cycling stability of Li–S batteries have been significantly increased to date thanks to the thoughtful design of nano-architectures and the strategic selection of functional host materials.[5–9]

Since separators must prevent polysulfide migration while enhancing electronic conductivity, they play a crucial role in anchoring polysulfides in Si–S batteries. Although a variety of carbon structures have been designed to function as efficient polysulfide traps, the adsorption capacity of these materials

[a] *Nanotechnology Research and Application Center – ITUnano, Istanbul Technical University, Maslak, Istanbul 34469, Turkey*
[b] *Center for BioNano Interactions, School of Chemistry, University College of Dublin, Belfield, Dublin 4, Ireland*
[c] *Department of Fluid Dynamics and Thermodynamics, Faculty of Mechanical Engineering, Czech Technical University in Prague, Prague 166 07, Czech Republic. E-mail: navid.aslfattahi@fs.cvut.cz*
[d] *Manisa Celal Bayar University, Bioengineering Department, Yunusemre, Manisa 45140, Turkey*
[e] *Energy Institute, Istanbul Technical University Maslak, Ayazaga Campus, Istanbul, Turkey*
[f] *Center for Advanced Mechanical and Green Technology, Center of Excellence for Robotics & Sensing Technologies, Faculty of Engineering and Technology, Multimedia University, Jalan Ayer Keroh Lama, 75450 Bukit Beruang, Melaka, Malaysia*
[g] *Faculty of Mechanical & Automotive Engineering Technology, University Malaysia Pahang Al-Sultan Abdullah, 26600 Pekan, Pahang, Malaysia. E-mail: kumaran@umpsa.edu.my*
[h] *Centre for Research in Advanced Fluid and Processes, University Malaysia Pahang Al-Sultan Abdullah, 26600 Pekan, Pahang, Malaysia*
[i] *Centre for Sustainable Materials & Surface Metamorphosis (CSMSM), Chennai Institute of Technology, Chennai, India*

† Electronic supplementary information (ESI) available. See DOI: https://doi.org/10.1039/d5cy00674k

is modest.[10–14] The strong chemical propensity of metal oxides and MXenes towards soluble polysulfides has been substantiated in their role as host materials. As such, the examination of hybrid hosts that incorporate carbon with MXenes presents a promising direction for the development of lithium–sulfur battery technology.

There are several possible uses for the $Ti_3C_2T_x$ MXene in Li–S batteries as a flexible current collector. Reports on the application of MXene films as an interlayer or separator in flexible batteries are currently lacking, underscoring the pressing need for a scalable process to create large-area $Ti_3C_2T_x$ films with high conductivity and polysulfides trapping.[15,16] Lithium polysulfides (LiPSs) are physically captured by the conductive carbon/MXenes, where the carbon component improves the separator's electrical conductivity. The polar LiPSs and the $Ti_3C_2T_x$ MXene/carbon materials in the upper layer have a strong interaction that successfully reduces the shuttle effect.[17,18]

The integration of various materials with MXene can mitigate the restacking of MXene nanosheets, improve the interaction with LiPSs, and expedite the sulfur redox reactions. MXene–carbon, MXene–metal compounds, MXene–polymer, MXene–organic framework and high-entropy MXene as a separator were summarized in Table S1.†

The study utilized carbon nanotubes (CNTs) to improve the high-rate capability and cycle life of $Ti_3C_2T_x$ as a coating on a glass fiber separator because of their exceptional electrical conductivity and mechanical strength. By connecting the horizontal $Ti_3C_2T_x$ layers and creating a conductive network on the surface, CNTs strengthen the internal structure of pre-lithiation Si–S batteries and lessen the shuttle effect. The high capacity of the $Ti_3C_2T_x$ MXene/CNT interlayer pre-lithiation Si–S battery is maintained at approximately 85% capacity even after 500 bending cycles.

Experimental section

Synthesis of the Si@GNP anode

A hydrothermal process was used to disperse Si NPs into an aqueous solution of GNP in order to create the Si/GNP nanostructure. Usually, 100 mL of deionized water was used to dissolve 7.5 g of GNP in order to create a homogenous solution. Following the addition of 0–1 g Si NPs to the solution above, the mixture was agitated for an hour. After being moved into a 100 ml Teflon-lined autoclave and maintained at 150 °C for 12 hours, the mixture was vacuum-filtered and washed with DI water. Prior to use, the Si@GNP electrode was subjected to a surface treatment and chemical pre-lithiation procedure in a glovebox filled with argon.

By treating the silicon anode with a pre-lithiation reagent, a stable artificial solid electrolyte interphase (SEI) film is formed, making chemical pre-lithiation a very effective technique for enhancing silicon anode performance. The electrolyte and anode material have less direct contact when this pre-formed SEI layer is present, which lessens unintended side reactions that occur during battery cycling. Chemical pre-lithiation also has a straightforward basic principle that allows for quick lithium replenishment and eliminates the need for slurry processing.

Lithium biphenyl/2-methyltetrahydrofuran (Li-BP/2-MeTHF) was used to prelithiate the Si@GNP anode to the necessary conditions in a matter of minutes. When Si@GNP is then coupled with the positive electrode, the cell's overall discharge capacity and rate capability show a significant improvement, even after a long cycle life.

Synthesis of $Ti_3C_2T_x$ MXenes

Lithium fluoride (325 mesh powder, 98.5% purity), hydrochloric acid (37 wt%), and MAX phase material (Ti_3AlC_2) were utilized in the synthesis of MXene ($Ti_3C_2T_x$) without any additional purification. 97.5% pure sodium hydroxide pellets were obtained from Fisher Chemicals. A 50 ml volume beaker was first filled with 15 ml of DI water and then 15 ml of HCl to create 30 ml of HCl (6 M). The HCl solution was then stirred for 30 minutes at 300 rpm while 3 g of LiF was added. To continue this etching process, 3 g of theMAX phase material (Ti_3AlC_2) was added to the solution gradually (within 15 minutes) to prevent overheating (an exothermic reaction). The resulting solution was then stirred for 48 hours at 40 °C. Following the etching procedure, a diluted solution of NaOH was gradually added until the pH of the mixture reached 6. The mixture was then filtered and repeatedly rinsed with deionized water. Using a centrifuge, the washing procedure was carried out four times at 3500 rpm for ten minutes each time. A vacuum oven was used to dry the multilayered MXene for the entire night.

Synthesis of the $Ti_3C_2T_x$/CNT interlayer

The single-walled carbon nanotubes (CNTs) were purchased from Sigma Aldrich. CNTs with carboxylic acid functionalization and purity of ≥90% was used. The length of 1.5 μm with a dimension of 5 nm was considered for synthesis.

A total of 100 mg of CNTs was introduced into 45 mL of a 1 wt% PVP solution, and sonicated for one hour to achieve a stable suspension with a concentration of 3 mg mL^{-1}. CNTs, and delaminated $Ti_3C_2T_x$ were combined in specific mass ratios (2 : 3) and sonicated for 30 minutes. The resulting suspension was then coated on one face of the glass fiber separator through the doctor blade slurry method. (Whatman glass microfiber 2.7 μm pore size white, 0.67 mm thick).

Finally, the $Ti_3C_2T_x$/CNT interlayer was carefully peeled off and placed in a vacuum oven at room temperature for 12 hours. Each interlayer had an approximate mass of 20 mg. For comparative purposes, the pure CNT interlayer was produced using the same methodology.

Cathode preparation

The sulfur cathode was created using the slurry method. Sulfur powder (S) and carbon black (CB) were first combined in a weight ratio of 75 wt% S, 15 wt% CB, and 10 wt% polyvinylidene fluoride (PVDF) in *N*-methyl-2-

pyrrolidone (NMP), placed in an agate mortar, and then ground to create a slurry. The doctor blade method was then used to coat the aluminum foil. For 12 hours, the coated cathode was dried at 60 °C in an air oven. The range of the S loading was 3.5–4.5 mg cm^{-2}.

Cell assembly and characterization

In a glove box filled with argon, the CR2032-type coin cells were put together using the S/CB cathode, $Ti_3C_2T_x$/CNT interlayer, Si@GNP anode, and electrolyte. An efficient electrolyte for polysulfide trapping was assessed in this work using a 1 M solution of bis(trifluoromethane)sulfonamide lithium (LiTFSI) and a 0.5 M solution of lithium nitrate ($LiNO_3$). In a 1 : 1 ratio, 1,3-dioxolane (DOL) and 1,2-dimethoxyethane (DME) made up the solvent mixture. The electrolyte volume was standardized at 20 μL per mg of sulfur.

Using a Neware BTS 3008 battery tester, the cells were cycled at room temperature between 1.5 and 3 V. Using a CHI660E electrochemical workstation, the electrochemical impedance spectroscopy (EIS) tests and cyclic voltammetry (CV) measurements were conducted from 100 KHz to 0.01 Hz at 1.5 V and with a scan rate of 0.1 mV s^{-1} in a potential range of 1.5–3 V. XRD diffraction analysis is performed using filter Cu Ka radiation (k = 1.541 Å) in a Rigaku SmartLab. A Renishaw Raman spectrometer was used to perform the Raman analysis, with a 532 nm argon laser serving as the exaction source. A Thermo Scientific K-Alpha XPS X-ray photoelectron spectrometer (Hemispherical analyzer) was used to analyze the elemental compositions. The samples were examined using transmission electron microscopy (TEM, JEOL JEM 2100F) and scanning electron microscopy (FESEM, ZEISS Gemini SEM 300) to describe their morphology. Using an energy-dispersive X-ray spectroscopy (EDS) SEM, the elemental distribution was examined. Through the use of thermogravimetry (TGA, SDT Q600) in an air atmosphere, the sulfur content was quantitatively examined. With the help of the lattice parameters derived from the TEM data, the geometry model was created. Stress strain experiments were performed utilizing a TriboIndenter (Hysitron Inc.) equipped with a three-sided pyramidal Berkovich diamond indenter. The resolutions for load and displacement are 100 nN and 0.1 nm, respectively. $Ti_3C_2T_x$/CNT and CNTs were evaluated by altering the maximum load while maintaining a loading and unloading rate of 200 mN s^{-1}.

Results and discussion

The synthesis pathway for the $Ti_3C_2T_x$/CNT interlayer is shown in Fig. 1. To create a stable suspension with a concentration of 3 mg mL^{-1}, 100 mg of CNTs were added to 45 mL of a 1 wt% PVP solution and sonicated for an hour. After combining CNTs and delaminated $Ti_3C_2T_x$ in precise mass ratios (40 : 60), they were sonicated for half an hour. The resulting suspension was then applied using the doctor blade slurry method to one face of the glass fiber separator. Lastly, the $Ti_3C_2T_x$/CNT interlayer was carefully peeled off and left in a vacuum oven at room temperature for 12 hours (Whatman glass microfiber, 2.7 μm pore size white, 0.67 mm thick). The mass of each interlayer was about 20 mg. The same process was used to create a pure CNT interlayer for comparison.

Using transmission electron microscopy (TEM) and scanning electron microscopy (SEM), the morphology of $Ti_3C_2T_x$ and CNTs is examined (Fig. 2a–d). It has a densely stacked lamellar structure, which increases the ion-accessible surface areas of the $Ti_3C_2T_x$ flakes by reducing their propensity to self-stack.[19–21] As illustrated in Fig. 2c–d, the interlaced CNTs form a network structure on the surfaces of $Ti_3C_2T_x$ upon their introduction. In addition to strengthening the adsorption of polysulfides onto the $Ti_3C_2T_x$ flakes and expanding their contact area, this special arrangement joins neighboring horizontal $Ti_3C_2T_x$ flakes in conjunction with the CNT.

SEM imaging in the cross-sectional mode is crucial for determining electrochemical characteristics. Cross-sectional SEM images of $Ti_3C_2T_x$/CNT showed the ordered, compact, and layered $Ti_3C_2T_x$ film as well as the porosity characteristics of a $Ti_3C_2T_x$/CNT composite.

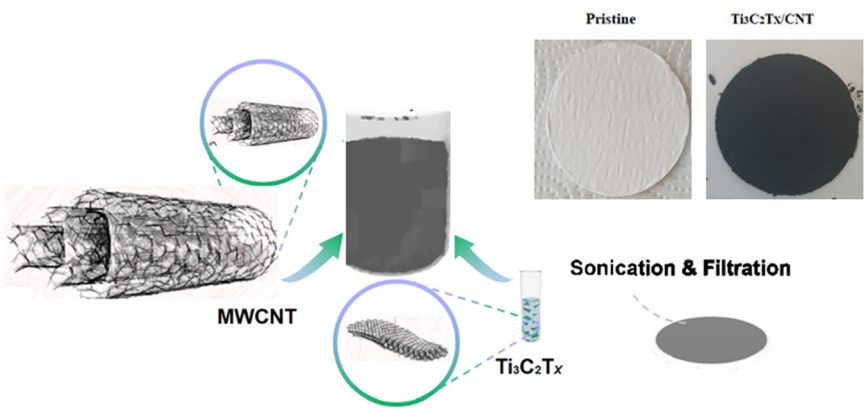

Fig. 1 Schematic illustration of the $Ti_3C_2T_x$/CNT preparation route.

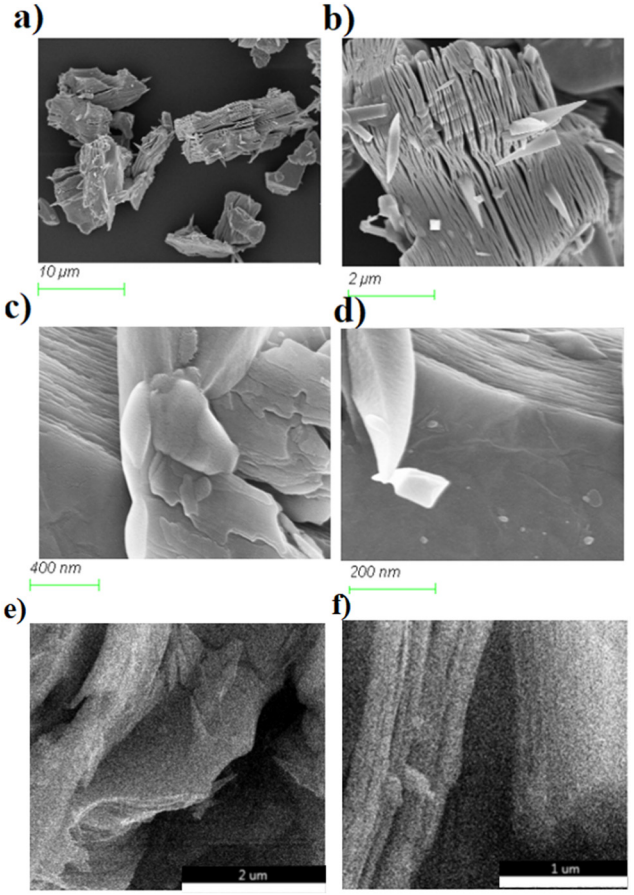

Fig. 2 a) and b) SEM images, c) and d) TEM images, and e) and f) cross-section SEM imaging of the $Ti_3C_2T_x$/CNT composite.

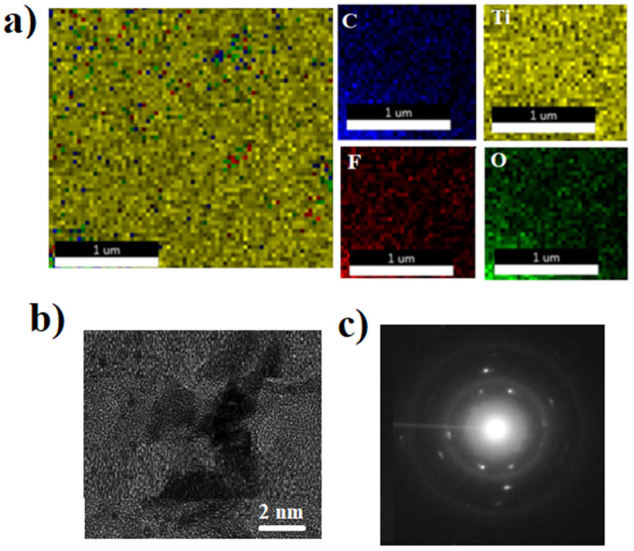

Fig. 3 a) EDS mappings, b) HRTEM image and c) SAED pattern of the $Ti_3C_2T_x$/CNT composite.

Ti and C are confirmed to be present in the $Ti_3C_2T_x$/CNT composite by the energy-dispersive X-ray spectroscopy (EDS) mappings shown in Fig. 3a. Furthermore, X-ray photoelectron spectroscopy (XPS) spectra highlight the presence of oxygen-related functional groups on the surface of the CNT. This shows the possibility of strong interfacial interactions between $Ti_3C_2T_x$ and CNTs, which are probably made possible by hydrogen bond formation. These interactions then interact with polysulfides to prevent polysulfide shuttle.[22–24] In addition, the HRTEM image of $Ti_3C_2T_x$/CNT composite confirms that MXene preserves its 2D cake-like morphology in the presence of the CNT and the intercalation of the CNT with MXene layers (Fig. 3b). The SAED pattern in Fig. 3c shows two phases: the CNT (diffraction ring) and retained MXene (hexagonal symmetry $Ti_3C_2T_x$).

Using X-ray diffraction (XRD), the phase composition of the films was examined. The intact layered structure of the two-dimensional $Ti_3C_2T_x$ flakes is demonstrated by the preserved (0 0 2) peak of $Ti_3C_2T_x$/CNT. Bragg's Law shows that the *d*-spacing of $Ti_3C_2T_x$ flakes has been successfully intercalated into the interlayer spaces between neighboring $Ti_3C_2T_x$ flakes, increasing from about 4.5 Å to about 7.0 Å (Fig. 4a). Diffraction peaks were found at angles of 26.5°, 34.1°, 43.2°, 51.2°, 54.6°, and 61.1°, which correspond to the rutile TiO_2 planes (110), (101), (111), (211), (220), and (301) (Fig. 4a).[25–28]

Raman spectra show two peaks at 1363 and 1589 cm^{-1} (Fig. 4b), which correspond to the D and G bands of carbon, indicating that carbon is an oxidation product of $Ti_3C_2T_x$/CNT. Small peaks that are associated with the vibrations of $Ti_3C_2T_x$ can also be found in the 200–600 cm^{-1} range.[29,30]

The porous structure of $Ti_3C_2T_x$/CNT was characterized using BET measurements. The isotherm of the $Ti_3C_2T_x$/CNT, as shown in Fig. 4c, shows a more noticeable hysteresis loop than that of CNTs, suggesting that CNTs were successfully incorporated into the $Ti_3C_2T_x$, which results in the interweaving of many micropores.[31,32]

Utilizing X-ray photoelectron spectroscopy (XPS), the elemental compositions and chemical bonding states of the $Ti_3C_2T_x$/CNT were examined (Fig. 5a).

TGA was used to assess the thermal stability of $Ti_3C_2T_x$/CNT (Fig. S1†). Up to 230 °C, the $Ti_3C_2T_x$/CNT maintains thermal stability; after that, its mass gradually decreases. Remaining water or removal of unstable surface functional groups (like –OH, ═O, and –F) is most likely the cause of this initial mass loss.[33–35] The reduction in weight between 230 °C and 390 °C is primarily due to the disproportionation reaction of $Ti_3C_2T_x$ MXene and its conversion into TiC, as evidenced by the XRD results.

$Ti_3C_2T_x$/CNT has a considerable number of –F groups, according to the Raman spectra, which are connected to the fluorine terminations on the $Ti_3C_2T_x$ flakes. The Ti–C peak at 282.8 eV found in the deconvoluted C 1s spectra (Fig. 5b) further confirms the presence of $Ti_3C_2T_x$. These oxygen-rich groups from CNT are also successfully retained in $Ti_3C_2T_x$, as evidenced by the presence of C–O (285.9 eV), C═O (286.3 eV), and COOH (287.9 eV).

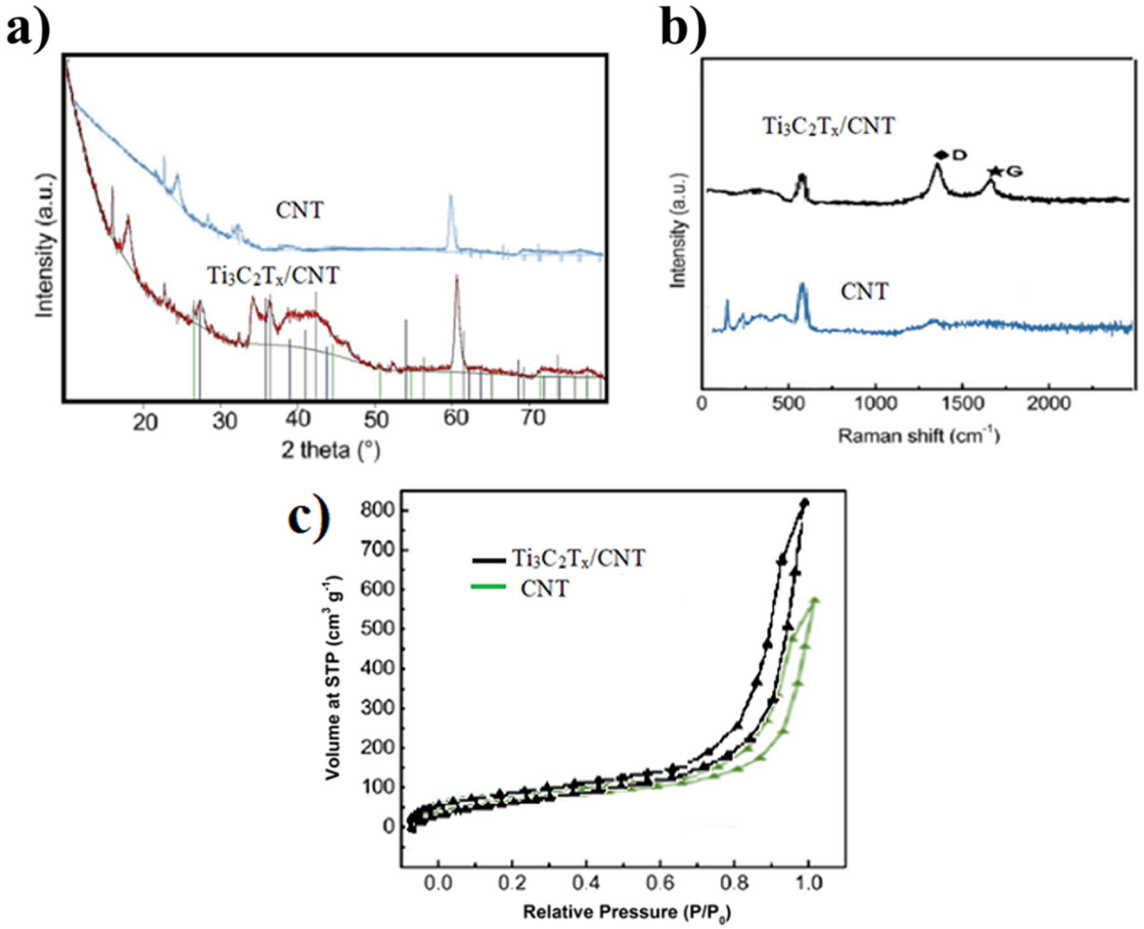

Fig. 4 a) XRD, b) Raman and c) BET analysis of $Ti_3C_2T_x$/CNT.

After oxidation, the TiO_2 peaks at 454.9 eV and 461.2 eV show a marked increase in intensity, as shown by XPS, indicating the formation of TiO_2 (Fig. 5c). These results are explained by a slight oxidation that is taking place on the surface of $Ti_3C_2T_x$.

$Ti_3C_2T_x$ is uniformly distributed throughout the CNT matrix leading to uniform volume changes during the lithiation and delithiation processes, which greatly diminish stress and strain while enhancing cycle life. This uniform distribution significantly reduces stress and strain while improving cycle life (Fig. S2†). To achieve a longer cycle life in the cell with the $Ti_3C_2T_x$/CNT interlayer, S/C cathode, and pre-lithiation Si anode, it is essential to reduce the stress and strain in $Ti_3C_2T_x$ within the CNT.

The cell with the $Ti_3C_2T_x$/CNT interlayer demonstrates superior cycling stability at a rate of 0.5 C over 500 cycles compared to the CNT interlayer. Its initial discharge capacity achieves 1391.6 mAh g^{-1} at 0.5 C, with an average capacity fade rate of only 0.079% per cycle over 500 cycles, significantly lower than the cell with CNT interlayer (0.114%) (Fig. 6a).

The exceptional architecture of $Ti_3C_2T_x$ in conjunction with CNTs offers a remarkable capacity of 1207.3 mAh g^{-1} at a rate of 0.2 C, in conjunction with a reversible capacity of 1047 mAh g^{-1} at 0.5 C. Following a sudden adjustment in the current rate from 1.0 C to 0.5 C and subsequently to 0.2 C, $Ti_3C_2T_x$/CNT demonstrated the capacity to rebound to 1027 and 1091 mAh g^{-1} respectively (Fig. 6b). High stability in capacity underscores the structural stability of $Ti_3C_2T_x$/CNT and the efficient LiPS adsorption properties of the $Ti_3C_2T_x$/CNT interlayer.

Fig. 6c depicts the charge–discharge behavior of the cell using $Ti_3C_2T_x$/CNT at a current density of 2C. The discharge capacities measured were 1371.8 mAh g^{-1}, 1203.4 mAh g^{-1}, 1174.8 mAh g^{-1}, 1051.7 mAh g^{-1}, and 989.8 mAh g^{-1} for the 1st, 20th, 50th 100th and 250th cycles, respectively, showing the creation of a solid electrolyte interphase (SEI) on the electrode's surface.[36]

Before and after 500 cycles, the electrochemical impedance spectroscopy (EIS) of the cell with the $Ti_3C_2T_x$/CNT interlayer, S/C cathode, and pre-lithiation Si anode was carried out at a rate of 0.5 C and in a voltage range of 1.5 to 2.8 V. 5. The EIS data wer fitted to an equivalent circuit in order to determine the ionic resistance (R_{st}) and charge transfer resistance (R_{ct}). Both the cathode and anode layers' interfacial resistances are linked to the charge transfer resistance (R_{ct}) in the entire cell. R_{ct} mostly results from electrolyte–cathode and interlayer interactions

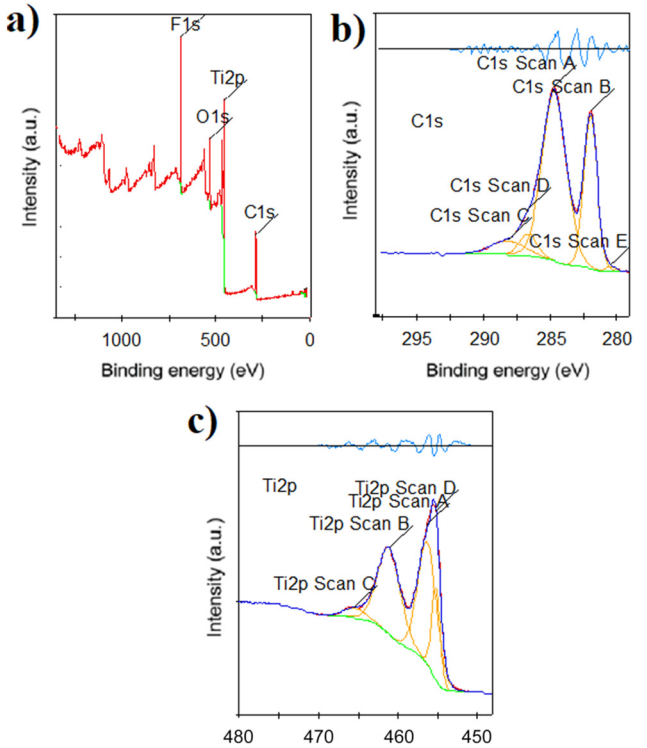

Fig. 5 a) XPS survey, b) C 1s and c) Ti 2p spectra of $Ti_3C_2T_x$/CNT.

and proves the good stability between the electrolyte and the pre-lithiation Si anode (Fig. 7a).[37]

The Nyquist curve of the fresh cell showed a single semicircle in both high and medium frequencies, along with a straight line in low frequencies. However, for the recycled cell at 500th cycle, an additional semicircle associated with the solid electrolyte interface (R_s) film towards solid polysulfides appears (Fig. 7a).[38]

After 500 cycles, a strong sulfur peak appeared in the $Ti_3C_2T_x$/CNT EDS spectrum, confirming that the interlayer had been successfully assembled for polysulfide trapping. $Ti_3C_2T_x$/CNT serves as a buffer to adapt to volume changes during cycling, which stops the shuttle of polysulfides, in addition to acting as a reservoir for polysulfides to improve electron transport into the active materials (Fig. 7b).

The SEM images after 500 cycles for the cells with pristine separator and $Ti_3C_2T_x$/CNT separator were presented in Fig. 8a and b. The cycled $Ti_3C_2T_x$/CNT separator is denser and thicker than those with pristine separator. Additionally, the cell with the $Ti_3C_2T_x$/CNT separator is more capable of producing robust polysulfides trapping film than pristine separator. This would be attributable to the distinct surface chemistry occurring due to the $Ti_3C_2T_x$/CNT anionic structure.[39]

After 500 cycles, the $Ti_3C_2T_x$/CNT EDS mapping (Fig. 8c) shows that the Ti elemental distribution closely resembles that of the C, S, and O elements, confirming the uniform distribution of $Ti_3C_2T_x$/polysulfides within the CNTs.

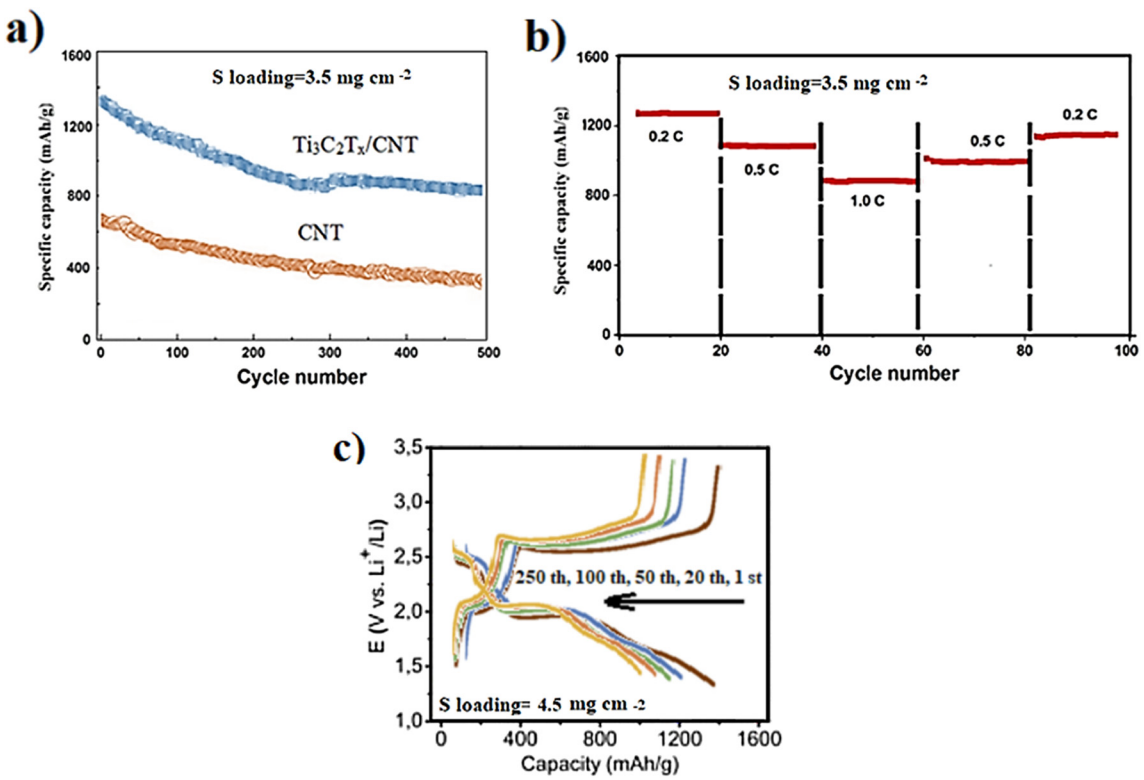

Fig. 6 a) Long cycle life of the cell with $Ti_3C_2T_x$/CNT and CNTs, b) rate performance of the cell with $Ti_3C_2T_x$/CNT and c) charge discharge voltage curve of the cell with $Ti_3C_2T_x$/CNT at 2C.

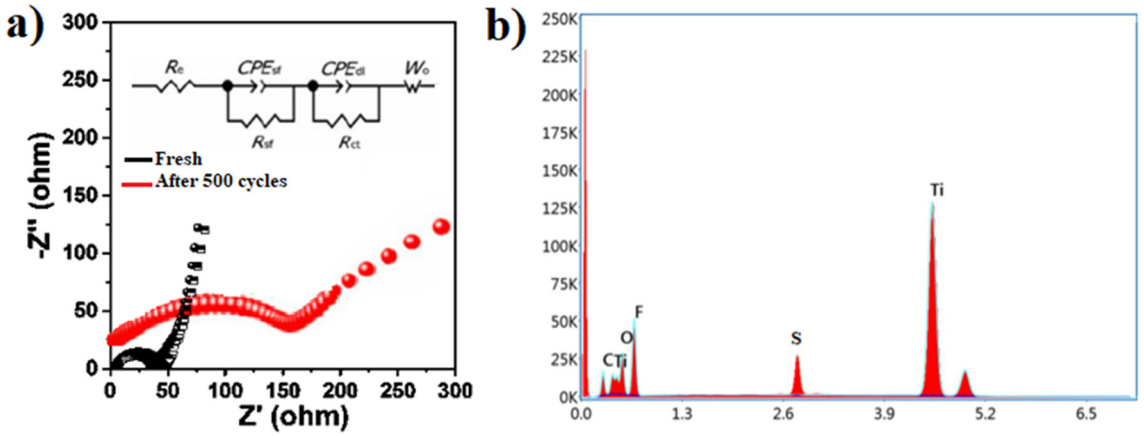

Fig. 7 a) Nyquist plots of the cell with $Ti_3C_2T_x$/CNT before and after 500 cycles and b) EDS spectrum of $Ti_3C_2T_x$/CNT after 500 cycles.

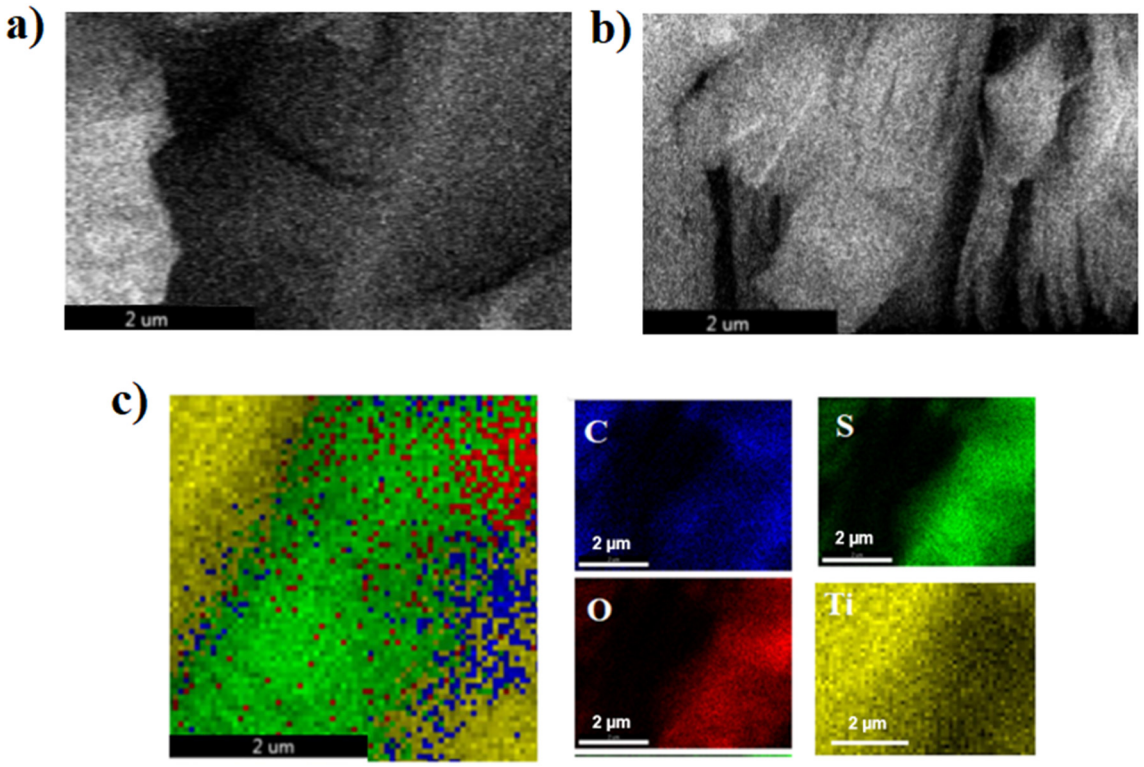

Fig. 8 SEM images of a) the pristine separator and b) $Ti_3C_2T_x$/CNT, and c) EDS elemental mapping of $Ti_3C_2T_x$/CNT after 500 cycles.

Fig. 9a shows that the battery with the pristine separator experience severe self-discharge, resulting in a capacity of 20% after resting for 100 hours at the 30th cycle. The battery using CNT and $Ti_3C_2T_x$/CNT separators have reasonable capacities of around 69% and 75% after resting for 100 hours at 30th cycle.

The study of the self-discharge mechanism with pristine, CNT and $Ti_3C_2T_x$/CNT separators was conducted and results showed that after a few hours, the OCV (2.31 V) of the battery with the pristine separator drops significantly, indicating serious self-discharge.

The CNT open circuit voltage (OCV) cell decreased by 2.41 V, after few hours resting, implying that the CNT is still capable of preventing the loss of active redox materials (Fig. 9b).

Using a $Ti_3C_2T_x$/CNT separator with higher OCV (2.45 V) after few hours effectively reduces self-discharge and matches the discharge capacity after several hours of rest (Fig. 9b).

DFT calculation

DFT calculations were conducted utilizing the PBE/def2-TZVP basis set. The binding energy per Li atom (E_{ad}) is determined using eqn (1).[40,41]

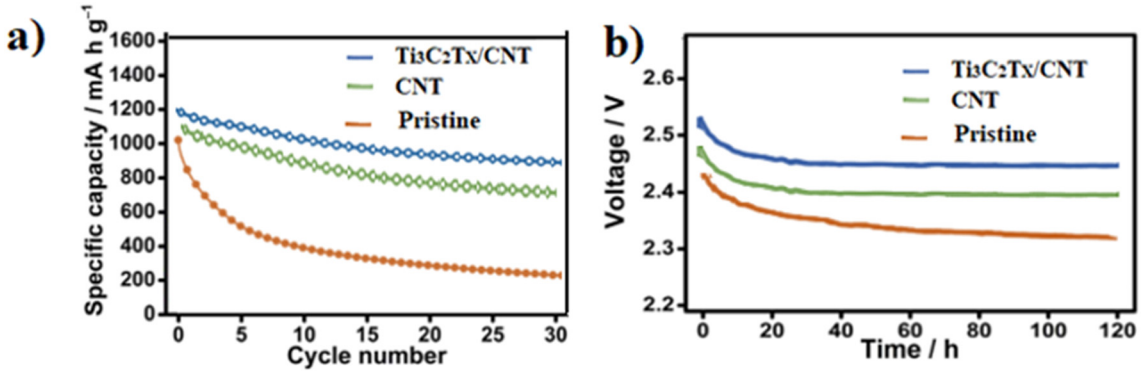

Fig. 9 a) Self discharge capacity and b) open circuit voltage profiles showing self-discharge behavior for pristine, CNT and $Ti_3C_2T_x$/CNT separators.

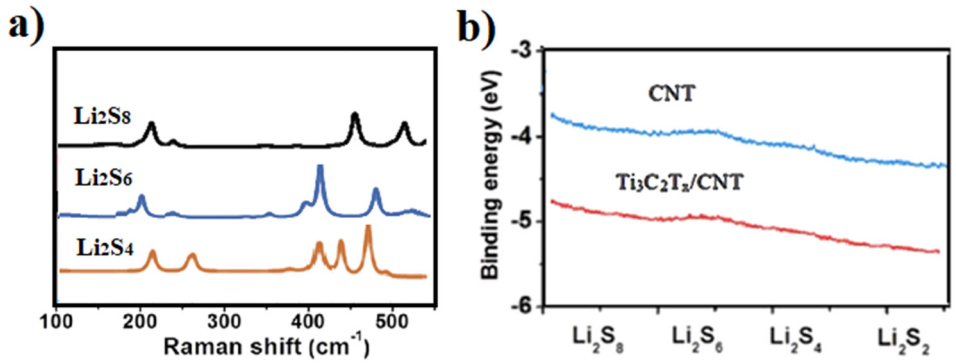

Fig. 10 a) Raman spectra of LiPSs and b) binding energies of various LiPSs on $Ti_3C_2T_x$/CNT and CNTs.

$$E_{ad} = \frac{E_{bonded} - E_{pristine} - 2\mu_{Li}}{2} \quad (1)$$

Here E_{ad} represents the energy values of the interaction between Li_2S_x (x = 2–8) and $Ti_3C_2T_x$/CNT, E_{total} represents that of the structure obtained as a result of optimization, $E_{molecule}$ represents that of Li_2S_x (x = 2–8), and $E_{MXene/CNT}$ represents that of the $Ti_3C_2T_x$/CNT structure.

Theoretical density functional theory (DFT) Raman spectra of LiPSs (Fig. 10a) were investigated to extract pertinent information through molecular dynamics simulation.

Fig. 10b illustrates the binding energies of various LiPSs that are adsorbed on different polysulfides. This indicates that the polar $Ti_3C_2T_x$/CNT demonstrates a significantly stronger anchoring capability for LiPSs in comparison to CNTs. Both CNT and $Ti_3C_2T_x$/CNT coated separators presented a catalytic mechanism in polysulfide conversion reactions and could enhance the redox reactions with trapping different polysulfides (Li_2S_x x = 2–8) (Fig. 10b).

Conclusion

On the surfaces of $Ti_3C_2T_x$, the interlaced CNTs form a network structure when they are introduced. This special arrangement joins neighboring horizontal $Ti_3C_2T_x$ flakes in conjunction with CNTs and ensures the adsorption of polysulfides onto the $Ti_3C_2T_x$ flakes, enhancing their contact area. At a rate of 0.5 C over 500 cycles, the cell with the $Ti_3C_2T_x$/CNT interlayer exhibits better cycling stability than the CNT interlayer with an average capacity fading rate of 0.079% per cycle. Following 500 cycles, the $Ti_3C_2T_x$/CNT EDS spectrum displayed a strong sulfur peak, confirming that the interlayer had been successfully assembled for the purpose of trapping polysulfides. In order to improve electron transport into the active materials, the $Ti_3C_2T_x$/CNT serves as a reservoir for polysulfides. It also acts as a buffer to adapt to volume changes during cycling, which stops polysulfide shuttle. These findings may offer novel synthetic strategies for the large-scale production of silicon-based anodes with modified MXene/CNT interlayers for upcoming Si–S batteries.

Data availability

Data will be available on a reasonable request from the corresponding author.

Author contributions

Conceptualization, Maryam Sadat Kiai; formal analysis, Maryam Sadat Kia, Navid Aslfattahi, Nilgun Baydogan, Deniz Karatas, Lingenthiran Samylingam, Kumaran Kadirgama,

and Chee Kuang Kok; investigation, Maryam Sadat Kiai, Deniz Karatas, and Chee Kuang Kok; methodology, Maryam Sadat Kiai, Navid Aslfattahi and Deniz Karatas; writing – original draft, Maryam Sadat Kia, Navid Aslfattahi, Nilgun Baydogan, Deniz Karatas, Lingenthiran Samylingam, Kumaran Kadirgama, and Chee Kuang Kok; writing – review & editing, Maryam Sadat Kia, Navid Aslfattahi, Nilgun Baydogan, Deniz Karatas, Lingenthiran Samylingam, Kumaran Kadirgama, and Chee Kuang Kok.

Conflicts of interest

Authors declare no competing interest.

Acknowledgements

All authors would like to thank Istanbul Technical University, Istanbul, University College of Dublin, Ireland, Czech Technical University in Prague, Czech Republic, Universiti Malaysia Pahang Al-Sultan Abdullah (UMPSA), Malaysia, and Multimedia University, Malaysia for resources and technical support.

References

1 M. S. Kiai, S. Ponnada, O. Eroglu, M. Mansoor, N. Aslfattahi, V. Nguyen, S. Gadkari and R. K. Sharma, *Dalton Trans.*, 2024, **53**, 82–92.
2 N. Aslfattahi, M. S. Kiai, N. Baydogan, L. Samylingam, K. Kadirgama and C. K. Kok, *Dalton Trans.*, 2025, **54**, 5100–5108.
3 N. Aslfattahi, M. S. Kiai, D. Karatas, N. Baydogan, L. Samylingam, K. Kadirgama and C. K. Kok, *Sustainable Energy Fuels*, 2025, **9**, 2137–2148.
4 N. Aslfattahi, M. S. Kiai, N. Baydogan, L. Samylingam, K. Kadirgama and C. K. Kok, *ACS Appl. Nano Mater.*, 2025, **16**(8), 8113–8121.
5 J. Zhang, H. Huang, J. Bae, S. H. Chung, W. Zhang, A. Manthiram and G. Yu, *Small Methods*, 2018, **2**, 1700279.
6 R. Pongilat, S. Franger and K. Nallathamby, *J. Phys. Chem. C*, 2018, **6**(122), 5948–5955.
7 Y. Q. Feng, Q. Q. Lu and H. Liu, *Tungsten*, 2024, **6**, 536–543.
8 J. Wu, Q. Ma, C. Lian, Y. Yuan and D. Long, *Chem. Eng. J.*, 2019, **15**(370), 556–564.
9 O. Eroglu, M. S. Kiai and H. Kizil, *J. Alloys Compd.*, 2020, **15**(838), 155607.
10 X. Liu, J. Q. Huang, Q. Zhang and L. Mai, *Adv. Mater.*, 2017, **29**, 1601759.
11 C. Song, Q. Yan, T. Zhang, H. Lin, H. Ye, Q. Yao, S. Zhang, Y. Li, G. Wang and J. Y. Lee, *Chem. Eng. J.*, 2021, **15**(420), 130452.
12 R. Mu, G. Suo, C. Lin, J. Li, S. Javed, X. Hou, X. Ye, Y. Yang and L. Zhang, *Chem. Eng. J.*, 2024, **15**(498), 155816.
13 Z. Hu, P. Gao, S. Ju, Y. Li, T. Zhang, C. Lu, T. Huang, P. Liu, Y. Lv, M. Guo and W. Zhang, *Nat. Commun.*, 2025, **2**(16), 1.
14 H. Wu, H. Wu, X. Ren, R. Li, H. Wang, W. Jia, Z. Lin, H. Liu, C. Xiong and L. Zhang, *Electrochim. Acta*, 2025, **1**(521), 145892.
15 X. Li, Y. Zhang, S. Wang, Y. Liu, Y. Ding, G. He, X. Jiang, W. Xiao and G. Yu, *Nano Lett.*, 2020, **20**, 6922–6929.
16 A. VahidMohammadi, J. Rosen and Y. A. Gogotsi, *Science*, 2021, **372**, 6547.
17 S. Wan, X. Li, Y. Chen, N. Liu, Y. Du, S. Dou, L. Jiang and Q. Cheng, *Science*, 2021, **1**(374), 96–99.
18 Q. Zhu, H. F. Xu, K. Shen, Y. Z. Zhang, B. Li and S. B. Yang, *Rare Met.*, 2022, **41**, 311–318.
19 W. Cao, C. Ma, S. Tan, M. Ma, P. Wan and F. Chen, *Nano-Micro Lett.*, 2019, **11**, 72.
20 P. Dutta, A. Sikdar, A. Majumdar, M. Borah, N. Padma, S. Ghosh and U. N. Maiti, *Carbon*, 2020, **1**(169), 225–234.
21 P. Pachfule, D. Shinde, M. Majumder and Q. Xu, *Nat. Chem.*, 2016, **8**, 718–724.
22 L. Jiao, C. Zhang, C. Geng, S. Wu, H. Li, W. Lv, Y. Tao, Z. Chen, G. Zhou, J. Li and G. Ling, *Adv. Energy Mater.*, 2019, **9**, 1900219.
23 G. Zhou, H. Tian, Y. Jin, X. Tao, B. Liu, R. Zhang, Z. W. She, D. Zhuo, Y. Liu, J. Sun and J. Zhao, *Proc. Natl. Acad. Sci. U. S. A.*, 2017, **31**(114), 840–845.
24 Z. W. Li, M. S. Han and J. Yu, *Rare Met.*, 2023, **42**, 3692–3704.
25 C. Wei, M. Tian, M. Wang, Z. Shi, L. Yu, S. Li, Z. Fan, R. Yang and J. Sun, *ACS Nano*, 2020, **6**(14), 16073–16084.
26 H. Li, H. Chen, Y. Xue, Y. Zhang, M. Zhang, W. Yu, G. Bai, K. Zhuo and Y. Zheng, *Adv. Energy Mater.*, 2020, **10**, 2001683.
27 Z. Zhang, D. Luo, G. Li, R. Gao, M. Li, S. Li, L. Zhao, H. Dou, G. Wen, S. Sy and Y. Hu, *Matter*, 2020, **2**(3), 920–934.
28 Y. Wang, R. Zhang, J. Chen, H. Wu, S. Lu, K. Wang, H. Li, C. J. Harris, K. Xi, R. V. Kumar and S. Ding, *Adv. Energy Mater.*, 2019, **9**, 1900953.
29 J. Tang, T. Mathis, X. Zhong, X. Xiao, H. Wang, M. Anayee, F. Pan, B. Xu and Y. Gogotsi, *Adv. Energy Mater.*, 2021, **11**, 2003025.
30 C. Zhao, G. L. Xu, Z. Yu, L. Zhang, I. Hwang, Y. X. Mo, Y. Ren, L. Cheng, C. J. Sun, Y. Ren and X. Zuo, *Nat. Nanotechnol.*, 2021, **16**, 166–173.
31 W. Yao, W. Zheng, J. Xu, C. Tian, K. Han, W. Sun and S. Xiao, *ACS Nano*, 2021, **25**(15), 7114–7130.
32 Z. Ye, Y. Jiang, L. Li, F. Wu and R. Chen, *Adv. Mater.*, 2021, **33**, 2101204.
33 B. Fei, C. Zhang, D. Cai, J. Zheng, Q. Chen, Y. Xie, L. Zhu, A. Cabot and H. Zhan, *ACS Nano*, 2021, **26**(15), 6849–6860.
34 D. Gueon, M. Y. Ju and J. H. Moon, *Proc. Natl. Acad. Sci. U. S. A.*, 2020, **9**(117), 12686–12692.
35 L. Shi, S. M. Bak, Z. Shadike, C. Wang, C. Niu, P. Northrup, H. Lee, A. Y. Baranovskiy, C. S. Anderson, J. Qin and S. Feng, *Energy Environ. Sci.*, 2020, **14**(13), 3620–3632.
36 P. Wu, L. Tan, X. D. Wang, P. Liao, Z. Liu, P. P. Hou, Q. Y. Zhou, X. J. Jin, M. C. Li, X. R. Shao and Z. Zeng, *Mater. Res. Bull.*, 2022, **1**(145), 111550.
37 Y. Tao, S. Chen, D. Liu, G. Peng, X. Yao and X. Xu, *J. Electrochem. Soc.*, 2015, **9**(163), A96.
38 H. Y. Wang, Y. K. Dai, K. M. Liao, S. Deng and G. P. Dai, *J. Phys. Chem. Lett.*, 2025, **23**(16), 1103–1113.

39 X. Ren, H. Wu, Y. Guo, H. Wei, H. Wu, H. Wang, Z. Lin, C. Xiong, H. Liu, L. Zhang and Z. Li, *Small*, 2024, **20**, 2312256.
40 D. Gueon, M. Y. Ju and J. H. Moon, *Proc. Natl. Acad. Sci. U. S. A.*, 2020, **9**(117), 12686–12692.
41 L. Shi, S. M. Bak, Z. Shadike, C. Wang, C. Niu, P. Northrup, H. Lee, A. Y. Baranovskiy, C. S. Anderson, J. Qin and S. Feng, *Energy Environ. Sci.*, 2020, **14**(13), 3620–3632.